Enhancing GNSS Positioning Accuracy for Road Monitoring Systems: A Factor Graph Optimization Approach Aided by Geospatial Information

Yihan Zhong, Runzhi Hu, *Graduate Student Member, IEEE*, Xiwei Bai, *Member, IEEE*, Xingxing Li, Li-Ta Hsu, *Senior Member, IEEE*, and Weisong Wen, *Member, IEEE*

Abstract— The global navigation satellite system (GNSS) is one of the most popular solutions to localize potential road cracks. Unfortunately, the accurate positioning of the GNSS in urban environments presents a significant challenge due to complex signal blockage and reflection phenomena. To tackle this, we propose a method that enhances GNSS positioning accuracy, particularly suited for the intricate layouts of urban canyons. Our approach integrates the prior map with lane line information into the factor graph optimization (FGO) algorithm, effectively mitigating the impacts of multipath effects and non-line-of-sight (NLOS). However, the poor accuracy of the initial guess from the GNSS positioning can easily lead to incorrect lane matching which is one of the main challenges of lane matching in highly urbanized areas. To fill this gap, this article proposes to use the switchable factor to model the potential incorrect lane matching by leveraging the redundancy of lane information across multi-epochs. This article verified the effectiveness of this methodology using two datasets from the dense urban environment of Hong Kong, collected using the low-cost automobile level receiver, and compared the results with conventional methods. Our findings affirm that integrating the FGO-based GNSS positioning system with map information significantly boosts positioning accuracy, demonstrating the robustness of our approach.

Index Terms— Factor graph optimization (FGO), geospatial information, global navigation satellite system (GNSS), map, navigation.

I. INTRODUCTION

A S TRAFFIC flow increases and roads and related infrastructure maintenance becomes costlier, urban road health monitoring becomes vital for ensuring traffic safety and sustaining city infrastructure [1], [2]. As the global urban population and economic activity expand, road infrastructure faces increasingly severe stress, necessitating periodic assessment and maintenance to guarantee smooth traffic flow and public safety [3]. Significant variations in road maintenance expenditure across different countries are evident. In 2021, the U.S. government allocated a substantial $110 billion to repair and update roads and bridges [4], while mainland China spent at least $15.1 billion on road maintenance [5]. Since 2015, the U.K. government has invested heavily in road repairs, including a $373 million fund from 16, 2015 to 21, 2020. In 2018, the U.K. injected a one-off sum of $529 million into highway maintenance across all road management departments in England [6]. In Hong Kong, the Highways Department reveals that the cost of road reconstruction over the past three years has exceeded $89 million [7]. These substantial investments highlight the importance of efficient and effective strategies for identifying and repairing road damage, with advanced road monitoring systems as a potential solution [8].

Road monitoring is vital for modern smart cities, as depicted in Fig. 1. A typical system begins with a vehicle integrated with sensors, such as cameras [9], [10] and LiDAR [11], [12], capable of perceiving the surrounding environment. It is also equipped with a global navigation satellite system (GNSS) receiver to provide the vehicle's position in the global coordinate system. When road damage is detected, the onboard computer reports the damaged location and uploads it to a cloud server. The control center then processes the received data and advises decision-making bodies on which roads require urgent repairs. Simultaneously, map service providers, such as Google Maps, can provide real-time alerts.

The effectiveness of these road monitoring systems heavily depends on accurate global positioning coordinates, which can be challenging to achieve in urban environments. As shown in Fig. 2, the number of visible satellites is limited due to obstruction by towering buildings, leading to multipath effects or non-line-of-sight (NLOS) receptions [13]. Moreover, the visible satellites typically align along the street direction, resulting in a high dilution of precision (DOP) value, indicative of poor satellite distribution. Hence, the role of GNSS positioning technology in urban road monitoring is crucial.

Yihan Zhong and Weisong Wen are with Hong Kong Polytechnic University Shenzhen Research Institute, Shenzhen, China, and also with the Department of Aeronautical and Aviation Engineering, The Hong Kong Polytechnic University, Hong Kong (e-mail: yi-han.zhong@connect.polyu.hk; welson.wen@polyu.edu.hk).

Runzhi Hu, Xiwei Bai, and Li-Ta Hsu are with the Department of Aeronautical and Aviation Engineering, The Hong Kong Polytechnic University, Hong Kong (e-mail: run-zhi.hu@connect.polyu.hk; xiwei.bai@connect.polyu.hk; lt.hsu@polyu.edu.hk).

Xingxing Li is with the School of Geodesy and Geomatics, Wuhan University, Wuhan, Hubei 430072, China (e-mail: xxli@sgg.whu.edu.cn).

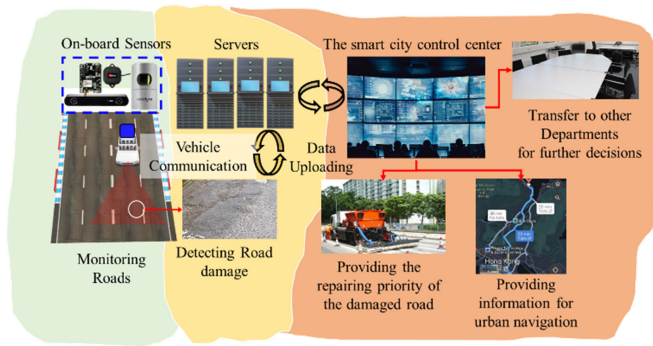Digital Object Identifier 10.1109/TIM.2024.3369156

Fig. 1.   Illustration of the road monitoring system in the context of smart cities.
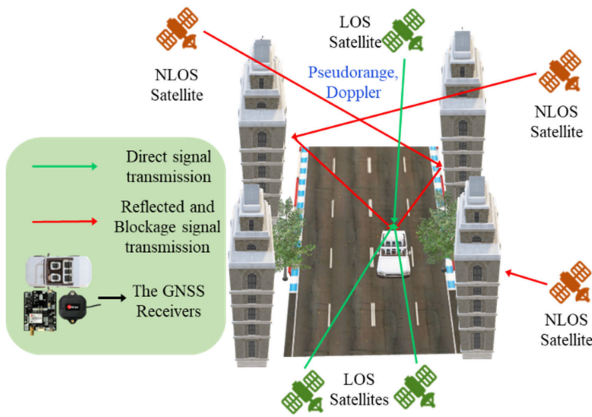

Fig. 2.   Problem of urban GNSS positioning.

There is growing interest in developing novel GNSS positioning technologies resilient to the complexities of urban environments. Accurate GNSS positioning technology can enable efficient resource utilization, leading to continuous improvements in urban road infrastructure. Real-Time Kinematic (RTK) is a high-precision GNSS positioning technique that utilizes carrier phase measurements to achieve centimeter-level accuracy [14], [15]. However, RTK's effectiveness in urban canyons is hampered by signal blockage, multipath effects, and the necessity for a nearby reference station to compute accurate differential corrections.

Recent research has explored using 3-D building models to aid GNSS positioning in urban canyons [16], [17], [18]. Despite the significant computational load introduced by 3-D building models, integrating lighter-weight data into the GNSS positioning system is deemed a more suitable approach for urban road monitoring systems. Thus, most vehicular navigation systems integrate the map-matching method [19]. One study proposed a map-aided GNSS positioning system designed to enhance positioning performance, considering various road types such as long straight roads, finite straight roads, and curved roads [20]. This research studies two cases: airplanes and vehicles [21]. In the case of vehicular positioning, a digital road map is used to match the driven path of the car to the road map, which improves the position to a meter-level accuracy. Another study integrated map information by using a priori approximate road network maps to build a hybrid metric and topological road map [22]. The map infor-

mation was fused to obtain more robust localization results. Furthermore, one study employed map data as an additional measurement in the filtering process by using it as a heading observation in a Kalman filter (KF) [23]. The OpenStreetMap (OSM) is a collaborative project that provides freely accessible and editable map data, including road networks [24]. OSM was first integrated into autonomous robot navigation in 2010 [25]. Interestingly, the OSM path was not used for positioning in this research, solely using the building information in OSM. Moreover, OSM also holds the potential for enhancing the indoor-outdoor scenario in tracking pedestrian movements [26]. By leveraging OSM data, GNSS positioning in urban canyons can be enhanced without expensive 3-D building models or computationally intensive processing. Nowadays, Google Earth Engine (GE) is popular as a geological resource [27]. Its utility spans various applications such as estimating daily blue ice fractions [28], monitoring temperate forest degradation [29], and assessing pasturelands and livestock dynamics [30]. GE can also aid in optimizing the path planning algorithm for minimal cost [31]. The precision of information within GE has been validated [32], [33], thus making it a viable tool for high-precision GNSS positioning. With the increasing availability of open data, the utilization of road information from GE becomes increasingly feasible.

In addition to integrating aided information, the framework for processing the measurements in the system is crucial for urban navigation. Weighted least squares (WLSs) and KF [34], [35], [36], [37] are conventional methods for GNSS positioning that have been widely adopted in various applications [38]. WLS is a linear estimation technique that minimizes the residuals between the observed and predicted measurements, while KF is a recursive filter that could estimate the state of a GNSS receiver based on noisy raw measurements. Both methods have inherent drawbacks, particularly in urban canyon environments. WLS is sensitive to outliers and may produce biased estimates in multipath and NLOS reception presence. On the other hand, KF relies on linear approximations and Gaussian noise assumptions, which may not adequately capture the complex signal environment in urban canyons [39]. Extended KF (EKF) is an extension of the KF that addresses the nonlinearity issue by linearizing the system model around the current state estimate [15]. While EKF has been employed to improve GNSS positioning in urban canyons more robust than KF, its performance is still limited by its recursive form and its reliance on Gaussian noise assumptions. To fill this gap, in today's GNSS positioning framework, factor graph optimization (FGO) has been well investigated recently which has proved its ability in the 2021 and 2022 Google Smartphone Decimeter Challenge (GSDC) [40], [41]. The winner employed the time difference carrier phase in FGO to obtain accurate relative positioning between epochs in his method. Integrating all the historical information and being free of the first-order Markov chain assumption improves FGO performance and lets it outperform EKF [42]. By employing comprehensive road information, FGO can consider vehicle motion constraints globally, resulting in more consistent positioning across the trajectory. Aiding road information can help reduce the accumulation of positioning errors and improve

overall positioning accuracy. In urban canyon environments, multipath effects and NLOS reception often affect GNSS signals, reducing positioning accuracy. By integrating map information, we can better solve these problems and make positioning results more robust to these influencing factors.

However, misaligned map matching in map-aided GNSS positioning introduces significant positioning errors, which is a critical problem that numerous reviews have documented [43], [44], [45]. Initial approaches to map-matching predominantly utilized straightforward techniques such as point-to-curve algorithms [46]. However, these early strategies are notably susceptible to inaccuracies resulting from suboptimal GNSS solutions. In response to these limitations, there have been innovative advancements in map-matching methodologies. For instance, one research team introduced a comprehensive approach that integrates data from multiple sources, including GNSS, dead reckoning (DR), and digital elevation models (DEM). This method employs the EKF to estimate the vehicle's position more accurately, which is then utilized for enhanced map-matching [47]. Significantly, this approach allows for the incorporation of additional attributes from links and nodes, providing a more nuanced and accurate mapping solution. Despite these advancements, it is vital to note that the prevalent issue of high GNSS noise in urban environments continues to challenge the efficacy of these methods, potentially leading to erroneous map-matching outcomes.

In addition to the errors introduced by GNSS outliers, trajectory outliers from the previous map can also result in incorrect state estimation [43]. By reviewing these studies, we aim to foster a broader understanding of map-matching inaccuracies and their impact on positioning precision. We also seek to demonstrate how our method parallels or deviates from these existing techniques.

Therefore, inspired by the performance of integrating additional map information and the characteristics of the advanced FGO framework, this article employs an FGO-based approach to tightly couple the road information from Google Earth with raw GNSS measurements to solve for the receiver's position. To the best of the authors' knowledge, this article is the first one that combines map information with GNSS raw measurements using FGO. The main contributions of this article are threefold.

1) *Multiepoch-Based Lane Matching Model Based on FGO:* This article proposed a novel FGO-based GNSS positioning system with a map-matching factor. The map-matching factor utilizes manually marked road information from Google Earth, a robust countermeasure against signal reflections and blockage in urban environments. This integration of geospatial data and FGO brings a new dimension to GNSS data processing and enhances the reliability of positioning in complex urban scenarios.

2) *Switchable Variable-Based Mis-Lane Matching Mitigation:* Recognizing the intricacy of urban environments, which often feature multiple lane lines, this article proposes the switchable factor for comprehensively considering the multiroads information. This factor aims to mitigate the potential for erroneous lane matching,
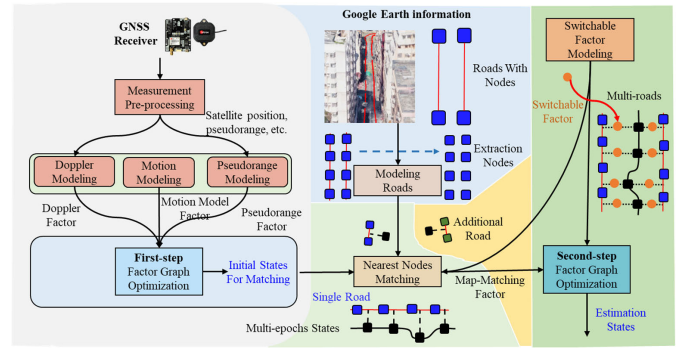

Fig. 3. Overview of the proposed system.

thereby enhancing the precision of our system. To succinctly explain, the switchable factor will represent this concept in the following text.

3) *Extensive Experimental Validation:* The proposed methodology is comprehensively validated using real-world data collected from Hong Kong. This rigorous empirical assessment underscores our commitment to ensuring our innovations' practical applicability and performance. The step-by-step validation process provides clear insights into the performance of our system, demonstrating its potential for improving GNSS positioning in the real world.

The remaining sections of this article are organized as follows: Section II is the overview of the proposed map-aided GNSS FGO positioning system. Then, the details of the modeled map factor and the switchable factor were proposed in Section III with modeling of GNSS measurements. Section IV presented the experiment setup and details of the collection data. Two experimental results in Hong Kong will be interpreted in Section V. Section VI presents discussions of the modeled map factor. Finally, Section VII presented conclusions and further work about the proposed FGO-based GNSS/GE integration.

II. SYSTEM OVERVIEW

Our proposed map-aided GNSS positioning method, as depicted in Fig. 3, leverages data from GE to improve the accuracy and reliability of GNSS positioning in urban canyons. The integrated GNSS/GE system consists of three primary components. The first component is the basic FGO part, which utilizes raw pseudorange and Doppler frequency measurements from the GNSS receiver. To ensure data quality, satellites with elevation angles (ELE) below 15° or signal-to-noise ratios (SNR) below 20 are excluded. The basic FGO part provides initial states for the matching part. The second component incorporates geospatial information from GE. We mark the lanes in GE and divide each road into multiple nodes. For each initial state, we determine the nearest nodes for matching. By identifying the closest road with nodes, we create a map-matching factor for each epoch state. This allows us to utilize multiepoch constraints for global lane alignment. Additionally, we propose a switchable factor to ensure reliable lane alignment. Unlike the previous map-matching factor,
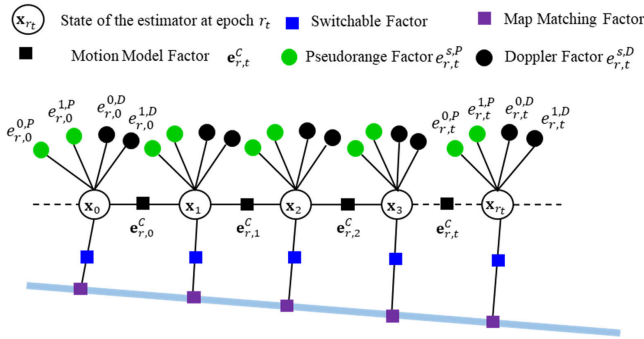
Fig. 4.   Overview of the proposed factor graph.

TABLE I
PARAMETERS AND THEIR DESCRIPTION IN THIS SECTION

Parameter name	Description
r	The GNSS receiver
s	The index of the satellite
t	The time epoch
$\rho_{r,t}^s$	The pseudorange measurement
$d_{r,t}^s$	The Doppler measurement
$rr_{r,t}^s$	The expected range rate
$\mathbf{p}_t^s$	The satellite position
	$\mathbf{p}_t^s = (p_{t,x}^s, p_{t,y}^s, p_{t,z}^s)^T$
$\mathbf{v}_t^s$	The velocity of the satellite
	$\mathbf{v}_t^s = (v_{t,x}^s, v_{t,y}^s, v_{t,z}^s)^T$
$\mathbf{p}_{r,t}$	The position of the GNSS receiver
	$\mathbf{p}_{r,t} = (p_{r,t,x}, p_{r,t,y}, p_{r,t,z})^T$
$\mathbf{v}_{r,t}$	The velocity of the GNSS receiver
	$\mathbf{v}_{r,t} = (v_{r,t,x}, v_{r,t,y}, v_{r,t,z})^T$
$\delta_{r,t}$	The clock bias of the GNSS receiver
$\delta_{r,t}^s$	The satellite clock bias by meters

the switchable factor provides more options for optimization by integrating two roads into the estimation simultaneously. The output of the GNSS/Map integration is the user's state estimation, which includes position, velocity, clock biases, and clock drift. The positioning solution is obtained by solving the optimization problem, incorporating various constraints and factors. These factors encompass the pseudorange, Doppler frequency, and motion model (MM) factor, which smooths the receiver's trajectory. Notably, we introduce a map-matching factor and switchable factor in this article, aligning the user's trajectory with the road network from Google Earth. This effectively mitigates the influence of multipath effects in urban canyons.

III. FGO-BASED GNSS/GE POSITIONING FRAMEWORK

A. Basic FGO Model

In this article, matrices are denoted in uppercase with bold letters. Vectors are denoted in lowercase with bold letters. Variable scalars are denoted as lowercase italic letters. Constant scalars are denoted as lowercase letters. Table I shows the descriptions of the parameters in this section for a clear explanation. Fig. 4 shows our proposed factor graph. The black, blue, and purple rectangular denote the MM factor, the switchable factor, and the map matching factor, respectively. The green and black circles denote the pseudorange and Doppler frequency factors, respectively. The subscript k denotes the total epochs of measurements considered in the FGO. The GNSS receiver state set is represented as follows:

$$\chi = [\mathbf{x}_{r,1}, \mathbf{x}_{r,2}, \ldots, \mathbf{x}_{r,k}] \tag{1}$$

$$\mathbf{x}_{r,t} = (\mathbf{p}_{r,t}, \mathbf{v}_{r,t}, \delta_{r,t}, \dot{\delta}_{r,t})^T \tag{2}$$

where the variable χ denotes the state set of the GNSS receiver ranging from the first epoch to the current k. $\mathbf{x}_{r,t}$ denotes the state of the GNSS receiver at epoch t which involves the position ($\mathbf{p}_{r,t}$), velocity ($\mathbf{v}_{r,t}$, receiver clock bias ($\delta_{r,t}$) and clock drift $\dot{\delta}_{r,t}$.

This article's main contribution is not the pseudorange, Doppler frequency, and MM factors [48], [49], [50]. Thus, this article will briefly introduce these three factors for estimating the initial pose in our proposed map-aided system. The GNSS pseudorange factor can be written as

$$\left\| \mathbf{e}_{r,t}^{s,P} \right\|_{\boldsymbol{\Sigma}_{r,t}^s}^2 = \left\| \rho_{r,t}^s - \left\| p_t^s - p_{r,t} \right\| - \delta_{r,t} \right\|_{\boldsymbol{\Sigma}_{r,t}^s}^2 \tag{3}$$

where $\omega_{r,t}^s$ denotes the noise, $\boldsymbol{\Sigma}_{r,t}^s$ denotes the covariance matrix, calculated using satellite SNR and ELE [51]. The Doppler frequency factor can be written as

$$\left\| \mathbf{e}_{r,k}^{s,D} \right\|_{\boldsymbol{\Sigma}_{r,t}^D}^2 = \left\| \lambda d_{r,t}^s - rr_{r,t}^s \right\|_{\boldsymbol{\Sigma}_{r,t}^D}^2 \tag{4}$$

where $\boldsymbol{\Sigma}_{r,t}^D$ denotes the covariance matrix corresponding to the Doppler measurement which is equal $\boldsymbol{\Sigma}_{r,t}^s$ multiplied by a fixed coefficient valued at 10. λ is the wavelength.

The MM factor is constructed for smoothing the vehicle trajectory. We can get the observation model for the smartphone-level GNSS receiver velocity ($\mathbf{v}_{r,t}$) expressed as follows:

$$\left\| \mathbf{e}_{r,t}^C \right\|_{\boldsymbol{\Sigma}_{r,t}^C}^2 = \left\| \Delta \mathbf{p}_{r,t} - (\mathbf{v}_{r,t} + \mathbf{v}_{r,t+1})/2 \right\|_{\boldsymbol{\Sigma}_{r,t}^C}^2 \tag{5}$$

where the $\mathbf{v}_{r,t}$ and $\mathbf{v}_{r,t+1}$ denote the velocity at two consecutive epochs with 3-D in the Earth-centered, Earth-fixed coordinate (ECEF) frame, respectively. $\Delta p_{r,t,x}, \Delta p_{r,t,y}, \Delta p_{r,t,z}$ denote the receiver displacement between two consecutive epochs at 3-D. $\boldsymbol{\Sigma}_{r,t}^C$ denotes the covariance matrix corresponding to the receiver velocity measurement. This article empirically [42] set $\boldsymbol{\Sigma}_{r,t}^C$ as follows:

$$\boldsymbol{\Sigma}_{r,t}^C = \begin{bmatrix} 0.3^2 & 0 & 0 \\ 0 & 0.3^2 & 0 \\ 0 & 0 & 0.3^2 \end{bmatrix} \tag{6}$$

where the unit for the covariance matrix is meter.

B. Incorporating GE Data in Multiepoch GNSS Positioning

This section describes the methodology for incorporating Google Earth data into our GNSS positioning technique to

improve accuracy and reliability in urban canyon environments.

First, we retrieve relevant road information from the Google Earth database to incorporate GE data and manually mark the road's latitude and longitude. The method we extract road information is similar to our previous work that extracting 3-D building models [52]. Initially, we ascertain the approximate lane ranges by conducting a comparative analysis with the terrain features depicted in GE. Subsequently, we refine the delineation of specific lanes through an iterative process, which involves a detailed comparison with the panoramic imagery available on Google Earth. The representation of the roadways is then accomplished by systematically plotting points along these identified lanes. The geographic coordinates (latitude and longitude) of these points are compiled to form a comprehensive dataset representing the specific lane information. Finally, we undertake a manual verification process to confirm the accuracy of the demarcated lanes, utilizing the camera data provided in the dataset [53] for validation. Thus, the road information can be denoted as follows:

$$\mathbf{R} = [\mathbf{R}_1, \mathbf{R}_2, \ldots, \mathbf{R}_n] \tag{7}$$

$$\mathbf{R}_n = \begin{bmatrix} l_{1,x}, l_{1,y} \\ l_{2,x}, l_{2,y} \\ \vdots \\ l_{m,x}, l_{m,y} \end{bmatrix} \tag{8}$$

where $\mathbf{R}$ denotes the matrix of road information and $\mathbf{R}_n$ denote the road with index n. $l_{m,x}$ and $l_{m,y}$ denote the longitude and latitude of the nodes of the road with the index m, respectively.

In the second step, we should consider incorporating road information into the optimization progress for better estimation based on the previously solved position. We can get the initial position for each epoch after solving the first-step optimization based on the previous GNSS factors and the MM factor. Once the initial position is determined, it is matched to the nearest two nodes by identifying the corresponding road indexes. Before we input these two roads into the map-matching factor, we should transform the coordinate system of the roads to ENU frame because we solely consider the horizontal errors in urban positioning. Then, we could employ a simple 2-D linear function for describing the chosen line in the ENU frame. So finally, we can derive the specified k and b for each line for the two selected lines.

Finally, the error functions of the map-matching factor can be written as follows:

$$\left\| \mathbf{e}_{r,k}^0 \right\|_{\mathbf{\Sigma}_{r,t}^{rd}}^2 = \left\| k_1 x^{ENU} - y^{ENU} + b_1 \right\|_{\mathbf{\Sigma}_{r,t}^{rd}}^2 \tag{9}$$

where the superscript 0 denotes the closest road, $[x^{ENU}, y^{ENU}]^T$ denote the horizontal state position to be estimated in the ENU frame. k_1 is the slope of the selected roads in the ENU coordinate system. b_1 is the intercept of the selected roads in the ENU coordinate system. $\mathbf{\Sigma}_{r,t}^{rd}$ denotes the covariance matrix of the map-matching factor.

C. Switchable Factor

In complex urban environments, relying solely on the position result of FGO to determine the matched road can

easily lead to incorrect matching. To comprehensively consider the possibility of multiple roads and fully leverage the map information in the FGO process, our method considers the information from the two nearest roads simultaneously during the optimization process. Therefore, the map-matching factor would add one more road to (8) and the aided factor can be written as

$$\left\| \mathbf{e}_{r,k}^1 \right\|_{\mathbf{\Sigma}_{r,t}^{rd}}^2 = \left\| k_2 x^{ENU} - y^{ENU} + b_2 \right\|_{\mathbf{\Sigma}_{r,t}^{rd}}^2 \tag{10}$$

where superscript 1 denotes the additional roads, $[x^{ENU}, y^{ENU}]^T$ denote the horizontal state position to be estimated in the ENU frame. k_2 is the slope of the selected roads in the ENU coordinate system. b_2 is the intercept of the selected roads in the ENU coordinate system. $\mathbf{\Sigma}_{r,t}^{rd}$ denotes the covariance matrix of the map-matching factor

$$\mathbf{\Sigma}_{r,t}^{rd} = \begin{bmatrix} 0.1^2 & 0 \\ 0 & 0.1^2 \end{bmatrix}. \tag{11}$$

This article considers the probabilities of multiroads with a switchable factor [54]. The switchable factor is utilized to anchor the switch variables at an initial value of 1, preventing the optimization process from getting stuck in a local minimum with all zero switch values. After aiding the switchable factor into the map-matching factor, the factor could be rewritten as

$$\left\| \mathbf{e}_{r,k}^0 \right\|_{\mathbf{\Sigma}_{r,t}^{rd}}^2 = s_k^i \left\| k_1 x^{ENU} - y^{ENU} + b_1 \right\|_{\mathbf{\Sigma}_{r,t}^{rd}}^2 \tag{12}$$

$$\left\| \mathbf{e}_{r,k}^1 \right\|_{\mathbf{\Sigma}_{r,t}^{rd}}^2 = \left(1 - s_k^i \right) \left\| k_2 x^{ENU} - y^{ENU} + b_2 \right\|_{\mathbf{\Sigma}_{r,t}^{rd}}^2 \tag{13}$$

where s_k^i denotes the switchable factor, the superscript i denotes the road index, and the subscript k denotes the epoch.

To avoid the switchable factor falling into a local minimum, we add the switchable prior factor into our framework [55], [56]

$$\left\| \mathbf{e}_{r,k}^s \right\|_{\mathbf{\Sigma}_{r,t}^s}^2 = \left\| 1 - s_k^i \right\|_{\mathbf{\Sigma}_{r,t}^s}^2 \tag{14}$$

where $\mathbf{\Sigma}_{r,t}^s$ is the covariance matrix of the switchable prior factor which equals 1.0.

Therefore, we can formulate the objective function for the map-aided FGO-based GNSS system based on the factors derived above as follows:

$$\chi^* = \arg \min_{\chi} \Sigma_{s,t} \left(\left\| \mathbf{e}_{r,t}^{s,P} \right\|_{\mathbf{\Sigma}_{r,t}^s}^2 + \left| \left| \mathbf{e}_{r,t}^C \right| \right|_{\mathbf{\Sigma}_{r,t}^C}^2 + \left\| \mathbf{e}_{r,k}^{s,D} \right\|_{\mathbf{\Sigma}_{r,t}^D}^2 \right. $$
$$\left. + \left\| \mathbf{e}_{r,k}^0 \right\|_{\mathbf{\Sigma}_{r,t}^{rd}}^2 + \left\| \mathbf{e}_{r,k}^1 \right\|_{\mathbf{\Sigma}_{r,t}^{rd}}^2 + \left\| \mathbf{e}_{r,k}^s \right\|_{\mathbf{\Sigma}_{r,t}^s}^2 \right). \tag{15}$$

The variable χ^* denotes the optimal estimation of the state sets. We employ the Ceres Solver [57] as a non-linear optimization solver to solve the above objective function. Concurrently, the Levenberg–Marquardt (L–M) algorithm [58] is utilized within our FGO processes to minimize the cost function iteratively.

In this article, we proposed two algorithms. The first algorithm is FGO-Matching which only considers one road information without switchable factors. The second algorithm is FGO-Switch which incorporates the road information with switchable factors. The detailed steps of FGO-Matching are

shown in the algorithm 1. The detailed steps of FGO-Switch are shown in Algorithm 2.

Algorithm 1 Solution to FGO-Matching

Inputs: Road information $\mathbf{R}$, GNSS measurements $\rho_{r,t}^s$ and $d_{r,t}^s$

Outputs: A set of state χ

Step 1 (Initialization): Initialize the state set χ using the weighted least squares and solve the following equation to estimate the state χ:

$$\chi^* = \underset{\chi}{arg min} \sum_{s,t}\left(\left\| \mathbf{e}_{r,t}^{s,P} \right\|_{\boldsymbol{\Sigma}_{r,t}^s}^2 + ||\mathbf{e}_{r,t}^C||_{\boldsymbol{\Sigma}_{r,t}^C}^2 + \left\| \mathbf{e}_{r,k}^{s,D} \right\|_{\boldsymbol{\Sigma}_{r,t}^D}^2 \right)$$

Step 2 (Matching): Select the nearest lane to the state χ from the road information in terms of calculating the closest point.

Step 3 (FGO-Matching): Solve the following equation to estimate the state χ

$$\chi^* = \underset{\chi}{arg min} \sum_{s,t}\left(\left\| \mathbf{e}_{r,t}^{s,P} \right\|_{\boldsymbol{\Sigma}_{r,t}^s}^2 + ||\mathbf{e}_{r,t}^C||_{\boldsymbol{\Sigma}_{r,t}^C}^2 + \left\| \mathbf{e}_{r,k}^{s,D} \right\|_{\boldsymbol{\Sigma}_{r,t}^D}^2 \right.$$
$$\left. + \left\| \mathbf{e}_{r,k}^0 \right\|_{\boldsymbol{\Sigma}_{r,t}^{rd}}^2 \right)$$

Algorithm 2 Solution to FGO-Switch

Inputs: Road information $\mathbf{R}$, GNSS measurements $\rho_{r,t}^s$ and $d_{r,t}^s$, a set of switchable variables $\mathbf{s}_k^i$

Outputs: A set of state χ and a set of switchable variables $\mathbf{s}_k^i$

Step 1 (Initialization): Initialize the switchable variables $\mathbf{s}_k^i$ with fixed value 1.0. Initialize the state set χ using the weighted least squares and solve the following equation to estimate the state χ:

$$\chi^* = \underset{\chi}{arg min} \sum_{s,t}\left(\left\| \mathbf{e}_{r,t}^{s,P} \right\|_{\boldsymbol{\Sigma}_{r,t}^s}^2 + ||\mathbf{e}_{r,t}^C||_{\boldsymbol{\Sigma}_{r,t}^C}^2 + \left\| \mathbf{e}_{r,k}^{s,D} \right\|_{\boldsymbol{\Sigma}_{r,t}^D}^2 \right)$$

Step 2 (Matching): Select the two nearest lanes to the state χ from the road information in terms of calculating the closest point.

Step 3 (FGO-Switch): Solve the following equation to estimate the state χ

$$\chi^* = \underset{\chi}{arg\,min} \Sigma_{s,t}(\left\| \mathbf{e}_{r,t}^{s,P} \right\|_{\boldsymbol{\Sigma}_{r,t}^s}^2 + ||\mathbf{e}_{r,t}^C||_{\boldsymbol{\Sigma}_{r,t}^C}^2 + \left\| \mathbf{e}_{r,k}^{s,D} \right\|_{\boldsymbol{\Sigma}_{r,t}^D}^2$$
$$+ \left\| \mathbf{e}_{r,k}^0 \right\|_{\boldsymbol{\Sigma}_{r,t}^{rd}}^2 + \left\| \mathbf{e}_{r,k}^1 \right\|_{\boldsymbol{\Sigma}_{r,t}^{rd}}^2 + \left\| \mathbf{e}_{r,k}^s \right\|_{\boldsymbol{\Sigma}_{r,t}^s}^2)$$

IV. EXPERIMENT SETUP

A. Sensor Configurations

To evaluate the performance of the proposed method, we gathered two datasets in a representative urban environment in Hong Kong. These two datasets show typical urban scenarios in Hong Kong, and we follow the definitions from [59]. The first dataset (Dataset 1) is gathered in deep urban, and another (Dataset 2) is collected in harsh urban. During the experiment, we utilized a u-blox F9P GNSS receiver to obtain raw GPS/BeiDou measurements at a frequency of 1 Hz. Additionally, the NovAtel SPAN-CPT, an integrated GNSS (GPS/GLONASS/BeiDou) RTK/INS fiber-optic gyroscopes (FOG) navigation system, provided ground truth (GT) positioning data. The FOG's gyro bias in-run stability is 1°/h, with a random walk of 0.067°/h. Prior to the experiments, the coordinate systems between all sensors were calibrated. Our data collection platform is shown in Fig. 5.

B. Collected Data in Hong Kong

Dataset 1 was collected in Whampoa, Hong Kong, a typical driving scenario due to the area's dense population and numerous residential districts. As a representative region of Hong Kong, vehicular GNSS positioning issues in this locale warrant considerable attention. We selected a random time slot during the day to gather data, with a collection length of nearly 1200 s. Fig. 6(a) demonstrates the variation in satellite count from the beginning to the end of the dataset's timeframe. As observed, in some extreme scenarios, the number of satellites is less than four, which is insufficient for GNSS positioning.
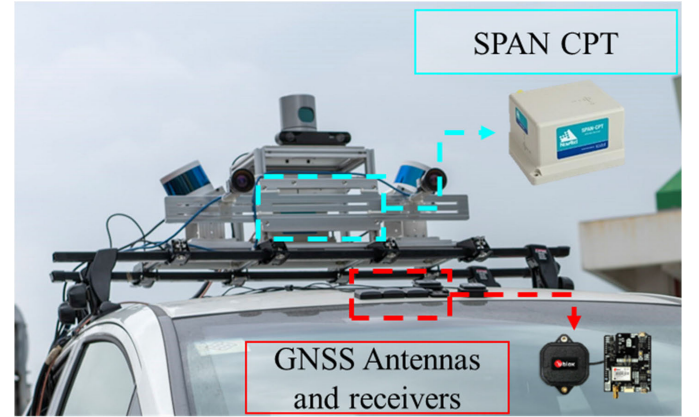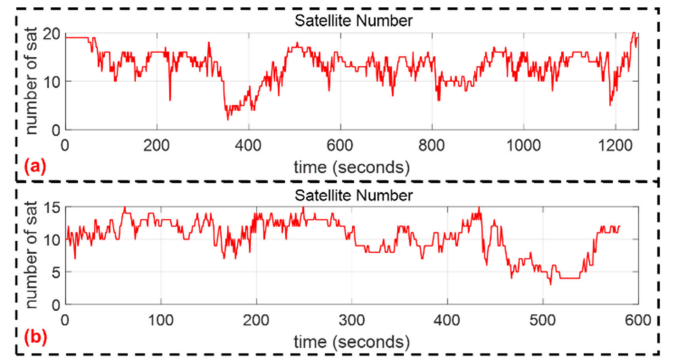

Fig. 5. Platform for the dataset collection.

Fig. 6. Number of satellites in two datasets. (a) Satellite number of Dataset 1. (b) Satellite number of Dataset 2.

Different from the first dataset, the second dataset (Dataset 2) is collected in Mangkok, Hong Kong. This scenario has more high-rise buildings. A reduced number of satellites
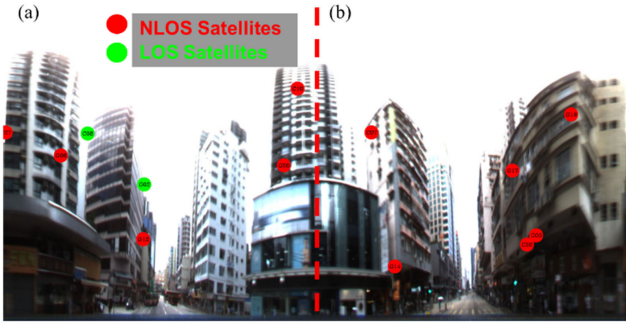
Fig. 7. Unfolded fish-eye camera figures with the satellite distributions in the urban canyon. (a) Street view directly in front of the vehicle. (b) Street view directly behind the vehicle.

Fig. 8. Trajectories overview of Dataset 1. (a) Overview. (b) Area A. (c) Area B.

Fig. 9. Trajectories overview of Dataset 2.

clearly illustrates this point. In the Whampoa dataset, the satellite count primarily fluctuates around 15, whereas in this dataset, it oscillates near 10, signifying a lower level of satellite redundancy. Fig. 6(b) shows the number of satellites in Dataset 2.

To further illustrate the difficulties of using GNSS positioning in urban canyons, we elucidate the issues in Dataset 1 by unfolding images from a fish-eye camera. As shown in Fig. 7, (a) represents the back 180° of the fish-eye camera, usually facing the rear of the vehicle, while (b) displays the satellite distribution in the vehicle's forward. Although the number of received satellites is sufficient in this scenario, it still contains numerous NLOS receptions or multipath effects. Red circles denote the NLOS satellites, and green circles denote the LOS satellites. These signals can result in GNSS positioning errors.

C. Evaluation Methods

We evaluated the performance of map-aided GNSS positioning by comparing three methods, as shown below. The objective of this analysis was to validate the effectiveness of the proposed method in improving FGO-based GNSS positioning. The accuracy is evaluated in the east, north, and up (ENU) frames by selecting the first point as the reference position.

1) *FGO [50]:* Conventional tightly coupled GNSS pseudorange/doppler frequency positioning solution. This method utilizes raw measurements from the GNSS receiver and optimizes the positioning solution based on conventional FGO [50].

2) *Three-Dimensional-Mapping-Aided (3DMA) [60]:* State-of-the-art urban GNSS positioning method. First, the WLS method is employed to obtain the initial guess of 3DMA. The sky masks of the corresponding areas can be generated based on the particles' location and the prior 3-D map. Then, the likelihood of each particle can be calculated by GNSS shadow matching. The predicted and measured satellite visibilities with the predicted and measured ranging measurements are considered. Finally, the absolute position can be calculated from the weighted average of the particles' positions. This 3DMA method is integrated with all constellations and L1/L2 frequency measurements.
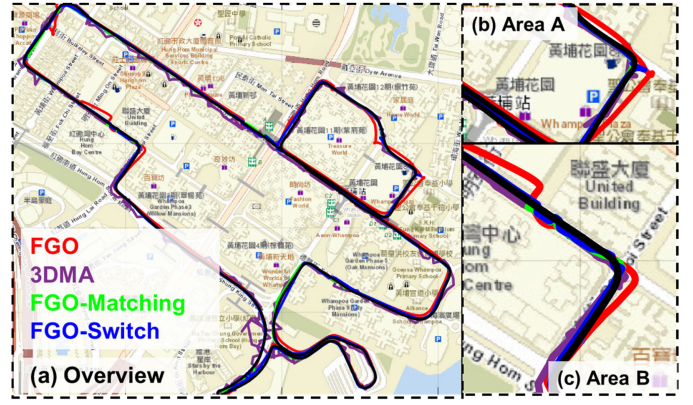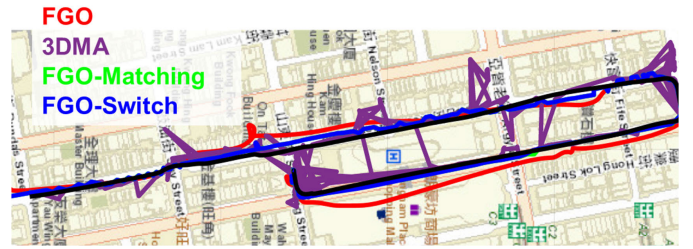
3) *FGO-Matching:* FGO-based GNSS positioning solution incorporating GE road data through a map-matching factor. This approach matches the initial positioning solution to the nearest road using road information from Google Earth.

4) *FGO-Switch:* FGO-Matching aided by a switchable factor for reliable road selection. This method considers the probabilities of both the closest roads in the map-matching process, utilizing a switchable factor for considering both roads, adding robustness and reliability to the positioning solution.

V. RESULTS

All methods in this article are post-processing methods. FGO-Switch typically runs 120% more than FGO-Matching with 3.3 s per epoch for FGO-Switch and 1.5 s per epoch for FGO-Matching in Dataset 1.

Fig. 8 illustrates the positioning trajectories of FGO, FGO-Matching, and FGO-Switch in Dataset 1, corresponding to red, green, and blue, respectively. The trajectories show that FGO is prone to erroneous positioning results in urban environments, causing the actual trajectory to deviate from city roads onto buildings. Fig. 8(b) and (c) show that FGO has a significant drift in these scenarios. In contrast, methods incorporating map matching can reduce errors in scenarios with severe drift, as evidenced by trajectories returning to the roadways.

Fig. 9 illustrates the positioning trajectories of FGO, FGO-Matching, and FGO-Switch in Dataset 2. Similar to the results in Dataset 1, FGO positioning yields erroneous results in more challenging urban environments, causing the actual positioning results to deviate from city roads and drift into buildings.

All Methods	RMSE (m)	MEAN (m)	STD (m)	MAX (m)
FGO	11.66	9.76	6.39	26.75
3DMA	10.91	8.41	6.95	58.45
FGO-Matching	10.47	8.63	5.92	27.62
FGO-Switch	10.11	8.34	5.71	26.50

All Methods	RMSE (m)	MEAN (m)	STD (m)	MAX (m)
FGO	15.02	12.31	8.62	29.03
3DMA	31.47	20.27	24.09	136.34
FGO-Matching	10.71	8.15	6.95	27.19
FGO-Switch	10.88	8.35	6.98	27.14

The 3DMA method shows larger errors than other FGO-based methods in this scenario. By incorporating map-matching methods, errors can be reduced even in cases of severe drift, as trajectories are readjusted to the roadways based on road information from Google Earth.

Table II presents the positioning error comparison in meters for Dataset 1, evaluating the performance of different methods, including FGO, FGO-Matching, 3DMA, and FGO-Switch. The metrics include root mean square error (RMSE), mean, standard deviation (STD), and maximum error (MAX). The 3DMA method shows a slight improvement over FGO and FGO-Matching, with an RMSE of 10.91 m and a mean error of 8.41 m. However, the STD increased to 6.95 m, indicating a slightly higher variability in the results. Notably, the MAX for 3DMA was significantly higher at 58.5 m, indicating occasional large deviations from the expected position. Compared to FGO, the FGO-Matching method demonstrates improvements in RMSE by 10.27%, mean by 11.52%, and STD by 7.41%. These improvements indicate that the FGO-Matching method provides superior accuracy and precision in positioning. However, the MAX increases slightly by -3.23%, suggesting that, in some instances, the FGO-Matching method might generate more significant errors than the FGO method. When comparing the FGO-Switch to the FGO method, we notice further enhancements in RMSE by 13.36%, mean by 14.55%, and STD by 10.63%. The result demonstrates that the FGO-Switch method further improves positioning accuracy and precision compared to FGO-Matching. Moreover, the MAX shows a marginal improvement of 0.95%, indicating that the FGO-Switch method can also effectively control the MAX. In summary, both FGO-Matching and FGO-Switch methods outperform the FGO method regarding positioning accuracy and precision. Furthermore, the FGO-Switch method appears to be more effective in controlling the MAX and offers slightly better overall improvements compared to the FGO-Matching method.

Table III presents the positioning error comparison in meters for Dataset 2. The 3DMA method exhibits relatively lower performance on this dataset compared to all FGO-based methods. A potential contributing factor could be the suboptimal initial estimates derived from the WLSs results, which may adversely affect the overall estimation accuracy. In a comparison against the FGO method, the FGO-Matching approach yields substantial improvements across several key metrics. We observed a decrease of 28.72% in the RMSE, 33.82% in the mean, and 19.30% in the STD. These improvements
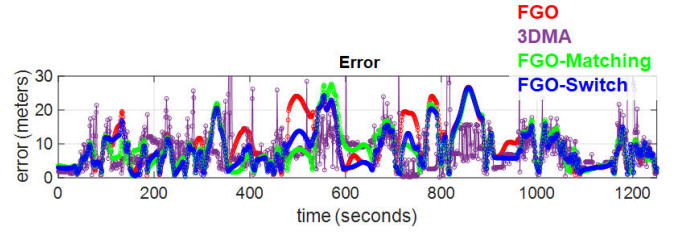

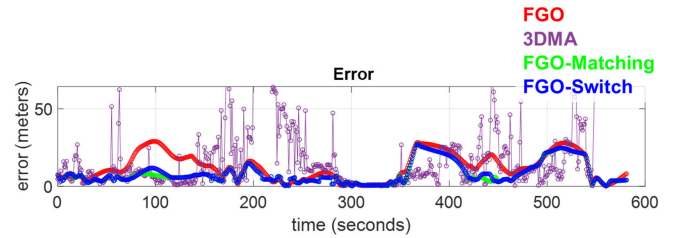Fig. 10. Two-dimensional positioning errors of three methods in Dataset 1.

Fig. 11. Two-dimensional positioning errors of three methods in Dataset 2.

suggest a significant enhancement in positioning accuracy and precision with the implementation of FGO-Matching for this dataset. The MAX also improved by 6.33%, indicative of the method's effectiveness in reducing the most significant positioning errors relative to the conventional FGO approach.

On the other hand, when analyzing the FGO-Switch method against the FGO approach, we also noted appreciable improvements. There was a reduction of 27.55% in RMSE, 32.14% in mean, and 18.98% in STD. These results demonstrate that FGO-Switch provides superior positioning accuracy and precision compared to the conventional FGO method. Furthermore, we also observed a slight improvement of 6.51% in the MAX, implying that the FGO-Switch method has a credible capacity to handle the MAX effectively. FGO-Matching has a better performance compared to the FGO-Switch. One potential reason for this suboptimal performance is similar to the 3DMA method that a bad initial guess for map-matching leading to erroneous estimation. This error could also be caused by the MM factor, leading to inaccurate global estimation. Although FGO-Matching performed slightly better regarding RMSE, mean, and STD, FGO-Switch has advantages in some cases. The primary advantage of FGO-Switch is that it effectively handles the potential problem of wrong map-matching by considering the probabilities of both roads using a switchable factor, which adds redundancy to the method.
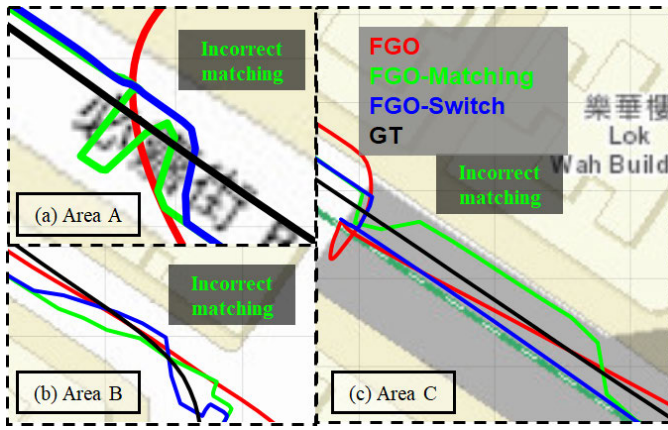
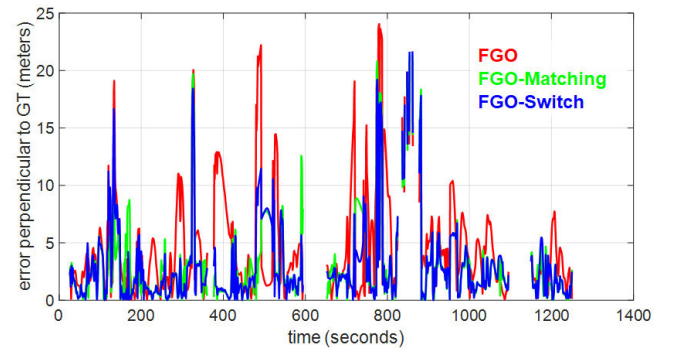Fig. 12. Comparison of three methods. (a) Area A. (b) Area B. (c) Area C.

Fig. 13. Two-dimensional positioning errors perpendicular to the GT direction of the three methods in Dataset 1.

TABLE IV
PERPENDICULAR ERRORS OF ALL METHODS IN DATASET 1

All Methods	RMSE (m)	MEAN (m)	STD (m)	MAX (m)
FGO	6.53	4.67	4.56	24.06
FGO-Matching	4.50	2.98	3.36	21.38
FGO-Switch	4.51	2.95	3.41	21.68

To better elucidate the error data listed in Tables II and III, Figs. 10 and 11 respectively display the trends of GNSS errors over time in the two datasets. As with the previously plotted trajectories, red, green, and blue denote FGO, FGO-Matching, and FGO-Switch, respectively. We can observe that between 400 and 700 s, both proposed methods exhibit significant improvements compared to the FGO, with a notable reduction in errors. This demonstrates that our proposed map-matching-based FGO method can effectively utilize the added map information to counteract the impact of GNSS outliers caused by multipath effects or NLOS receptions.

Fig. 11 shows the performance of the three evaluation methods in Dataset 2. Our proposed approach demonstrates more significant optimization in this scenario. The error of FGO (red curve) reaches around 30 m at approximately 100 s, while by incorporating lane constraints from the map in the optimization process, we can observe that both FGO-Matching and FGO-Switch effectively resist outliers, with errors distributed around 10 m.

VI. DISCUSSION

This article demonstrates that incorporating the switchable factor into our GNSS positioning system is instrumental in accurately selecting the correct lane for the estimated trajectories. Fig. 12 compares the trajectories of three methods: FGO, FGO-Matching, and FGO-Switch. The red circle means the scenario in FGO-matching chose the wrong road. Fig. 12(a)–(c) all show the estimated trajectories for the respective method alongside the ground truth trajectory. Compared to the FGO and the FGO-Matching methods, we can observe that the FGO-Switch method achieves better lane selection and positioning accuracy. By integrating the switchable factor, the FGO-Switch method can effectively weigh the probability of the vehicle being on two adjacent lanes, enabling it to select the correct lane more consistently. The switchable factor is a constraint that prevents reliable lane selection. In conclusion, Fig. 12 provides strong evidence that incorporating the switchable factor into our GNSS positioning system significantly improves the accuracy of lane selection, leading to better overall positioning performance in urban environments.

Fig. 13 illustrates the error values associated with three distinct methods, measured in a direction perpendicular to the

GT. It is essential to highlight that these evaluations were limited to dynamic scenes due to the absence of a motion direction in static scenarios. The figure shows a significant fluctuation in the error curve associated with the FGO method (represented by the red curve). Notably, the peak value of this curve markedly surpasses that of the method incorporating map matching. In contrast, FGO-Switch (depicted by the blue curve) demonstrates superior performance compared to FGO-Matching at approximately 200 and 600 s. This pattern suggests that our proposed switchable factor can more effectively facilitate vehicle lane-matching within this context.

As illustrated in Table IV, the RMSE was 6.53 m, the mean error was 4.67 m, the STD was 4.56 m, and the MAX value was 24.06 m for the FGO method. In comparison, the FGO-Matching method yielded substantial improvements across all metrics. The RMSE decreased to 4.50 m, representing a reduction of 31.12%. The mean error correspondingly decreased to 2.98 m, signifying an improvement of 36.07%. Moreover, the STD, which serves as a statistical indicator of error dispersion, declined to 3.36 m, denoting an enhancement of 26.29%. The MAX also observed a decrease to 21.38 m, marking an improvement of 11.15%.

On the other hand, our proposed FGO-Switch method exhibited performance metrics akin to those of the FGO-Matching method. Although the RMSE was marginally higher at 4.51 m, it still signified a 30.97% improvement over the traditional FGO method. The mean error slightly decreased to 2.95 m, indicating an improvement of 36.85%. The STD increased marginally to 3.41 m, yet it still represented an improvement of 25.30% over the FGO method. The MAX was also slightly larger at 21.68 m, but it denoted a 9.88% improvement compared to the FGO method.

In summary, FGO-Matching and FGO-Switch methods substantially improve over the conventional FGO method. However, it is pertinent to underscore that the FGO-Switch

TABLE V
PERPENDICULAR ERRORS OF ALL METHODS IN DATASET 2

All Methods	RMSE (m)	MEAN (m)	STD (m)	MAX (m)
FGO	10.72	8.38	6.70	27.25
FGO-Matching	7.50	4.84	5.73	25.31
FGO-Switch	7.53	4.91	5.72	25.32

method demonstrated a minor improvement in mean error when compared to the FGO-Matching method, suggesting its potential for superior accuracy in lane-level localization.

Based on Table V results, the FGO method yielded an RMSE of 10.72, a mean error of 8.38, an STD of 6.70, and an MAX of 27.25. In contrast, the FGO-Matching method demonstrated significant improvements in all metrics compared to the conventional FGO method. The RMSE was reduced to 7.50 m, signifying a decrease of 30.07%. Additionally, the mean error reduced considerably to 4.84 m, marking a 42.18% improvement. The STD decreased to 5.73 m, indicating a 14.48% improvement. Similarly, the MAX experienced a reduction to 25.31 m, an improvement of 7.10%. The FGO-Switch method showed performance metrics akin to those of the FGO-Matching method. Despite a slight increase in the RMSE to 7.53 m, it still represented a 29.73% improvement over the FGO method. The mean also increased marginally to 4.91 but showed a substantial 41.38% improvement. The STD remained nearly consistent at 5.72 m, showing a 14.61% improvement, while the MAX, though marginally higher at 25.32 m, still represented a 7.08% improvement over the FGO method. Similar to the Dataset 1 result, both the FGO-Matching and FGO-Switch methods significantly supersede the performance of the traditional FGO method across all metrics. However, the marginal difference between the FGO-Matching and FGO-Switch methods suggests comparable effectiveness in reducing the errors perpendicular to the GT.

VII. CONCLUSION

This article presents a novel method for enhancing the accuracy of urban GNSS positioning that suffered multipath effects and NLOS receptions. Our approach integrates multiepoch human-marked lane information from GE into an FGO-based method as a map, and its efficacy in improving the GNSS positioning performance was validated using two real-world datasets. Furthermore, we introduced a switchable factor to enhance the reliability of map matching. Our results demonstrate that the proposed FGO-Matching and FGO-Switch methods achieved superior positioning accuracy compared to the conventional FGO method in the validated challenging urban environments. Moreover, our approach provides a practical solution for urban road monitoring applications requiring precise positioning data. We observed an increase of approximately 120% in computation time compared to the original algorithm. Despite this increment, the overall efficiency of the algorithm remains within acceptable limits for practical applications. However, when the initial guess is bad, FGO-Switch shows lower robustness than FGO-Matching because a bad initial guess leads to erroneous map-matching.

These errors would be integrated into the estimation process and the MM factor will potentially propagate these errors.

Currently, we only employ GPS/BeiDou L1 frequency pseudorange and Doppler Frequency in our algorithm. To fill this gap, we will consider more frequency and constellations messages, and consider incorporating carrier-phase for better measurements redundancy in the future. Besides, we will also integrate the inertial measurement units (IMU) for urban localization to eliminate the errors from MM factors. Additionally, the approach can be expanded to include other types of data, such as vehicle-to-everything (V2X) communication and sensor fusion techniques, to bolster positioning accuracy and reliability further.

REFERENCES

[1] T. Dózsa, J. Radó, J. Volk, Á. Kisari, A. Soumelidis, and P. Kovács, "Road abnormality detection using piezoresistive force sensors and adaptive signal models," *IEEE Trans. Instrum. Meas.*, vol. 71, pp. 1–11, 2022.

[2] A. S. El-Wakeel, J. Li, A. Noureldin, H. S. Hassanein, and N. Zorba, "Towards a practical crowdsensing system for road surface conditions monitoring," *IEEE Internet Things J.*, vol. 5, no. 6, pp. 4672–4685, Dec. 2018, doi: 10.1109/JIOT.2018.2807408.

[3] X. Huang, D. Wen, J. Li, and R. Qin, "Multi-level monitoring of subtle urban changes for the megacities of China using high-resolution multi-view satellite imagery," *Remote Sens. Environ.*, vol. 196, pp. 56–75, Jul. 2017.

[4] TW HOUSE. (2021). *Fact Sheet: The Bipartisan Infrastructure Deal*. [Online]. Available: https://www.whitehouse.gov/briefing-room/statements-releases/2021/11/06/fact-sheet-the-bipartisan-infrastructure-deal/#:~:text=The%20legislation%20will%20reauthorize%20surface,and%20support%20major%2C%20transformational%20projects

[5] MOTOTPSRO China. (2020). *Notification of the Ministry of Transport on the Issuance of the '14th Five-Year' Highway Maintenance Management Development Outline*. [Online]. Available: https://xxgk.mot.gov.cn/2020/jigou/glj/202204/t20220426_3652905.html

[6] BVON Department for Transport. (Feb. 15, 2021). *Funding To Fix Equivalent of 10 Million Potholes Allocated To Local Authorities*. [Online]. Available: https://www.gov.uk/government/news/funding-to-fix-equivalent-of-10-million-potholes-allocated-to-local-authorities

[7] HDOHKSA Region. (2023). *Road Resurfacing Works Completed in Past 3 Years*. [Online]. Available: https://www.hyd.gov.hk/en/our_services/road_resurfacing_works/works_completed.html

[8] A. Gharaibeh et al., "Smart cities: A survey on data management, security, and enabling technologies," *IEEE Commun. Surveys Tuts.*, vol. 19, no. 4, pp. 2456–2501, 4th Quart., 2017.

[9] X. Bai, W. Wen, and L.-T. Hsu, "Degeneration-aware outlier mitigation for visual inertial integrated navigation system in urban canyons," *IEEE Trans. Instrum. Meas.*, vol. 70, pp. 1–15, 2021.

[10] Q. Li and S. Ren, "A real-time visual inspection system for discrete surface defects of rail heads," *IEEE Trans. Instrum. Meas.*, vol. 61, no. 8, pp. 2189–2199, Aug. 2012, doi: 10.1109/TIM.2012.2184959.

[11] G. He, X. Yuan, Y. Zhuang, and H. Hu, "An integrated GNSS/LiDAR-SLAM pose estimation framework for large-scale map building in partially GNSS-denied environments," *IEEE Trans. Instrum. Meas.*, vol. 70, pp. 1–9, 2021.

[12] H. Li, B. Tian, H. Shen, and J. Lu, "An intensity-augmented LiDAR-inertial SLAM for solid-state LiDARs in degenerated environments," *IEEE Trans. Instrum. Meas.*, vol. 71, pp. 1–10, 2022.

[13] P. D. Groves, "Principles of GNSS, inertial, and multisensor integrated navigation systems, 2nd edition [book review]," *IEEE Aerosp. Electron. Syst. Mag.*, vol. 30, no. 2, pp. 26–27, Feb. 2015, doi: 10.1109/MAES.2014.14110.

[14] R. B. Langley, "RTK GPS," *GPS World*, vol. 9, no. 9, pp. 70–76, 1998.

[15] T. Takasu and A. Yasuda, "Development of the low-cost RTK-GPS receiver with an open source program package RTKLIB," in *Proc. Int. Symp. GPS/GNSS*, South Korea, vol. 1, 2009, pp. 1–6.

[16] P. D. Groves, "Shadow matching: A new GNSS positioning technique for urban canyons," *J. Navig.*, vol. 64, no. 3, pp. 417–430, Jun. 2011, doi: 10.1017/S0373463311000087.

[17] L.-T. Hsu, Y. Gu, and S. Kamijo, "3D building model-based pedestrian positioning method using GPS/GLONASS/QZSS and its reliability calculation," *GPS Solutions*, vol. 20, no. 3, pp. 413–428, Jul. 2016.

[18] Y. Wada, L.-T. Hsu, Y. Gu, and S. Kamijo, "Optimization of 3D building models by GPS measurements," *GPS Solutions*, vol. 21, no. 1, pp. 65–78, Jan. 2017, doi: 10.1007/s10291-015-0504-y.

[19] F. Marchal, J. Hackney, and K. W. Axhausen, "Efficient map matching of large global positioning system data sets: Tests on speed-monitoring experiment in zürich," *Transp. Res. Rec., J. Transp. Res. Board*, vol. 1935, no. 1, pp. 93–100, Jan. 2005.

[20] C. Scott, "Improved GPS positioning for motor vehicles through map matching," in *Proc. 7th Int. Tech. Meeting Satell. Division Inst. Navigat. (ION GPS)*, 1994, pp. 1391–1400.

[21] F. Gustafsson et al., "Particle filters for positioning, navigation, and tracking," *IEEE Trans. Signal Process.*, vol. 50, no. 2, pp. 425–437, Feb. 2002.

[22] K. W. Lee, S. Wijesoma, and J. I. Guzmán, "A constrained SLAM approach to robust and accurate localisation of autonomous ground vehicles," *Robot. Auto. Syst.*, vol. 55, no. 7, pp. 527–540, Jul. 2007.

[23] C. Fouque, P. Bonnifait, and D. Betaille, "Enhancement of global vehicle localization using navigable road maps and dead-reckoning," in *Proc. IEEE/ION Position, Location Navigat. Symp.*, 2008, pp. 1286–1291.

[24] M. Haklay and P. Weber, "OpenStreetMap: User-generated street maps," *IEEE Pervasive Comput.*, vol. 7, no. 4, pp. 12–18, Oct. 2008.

[25] M. Hentschel and B. Wagner, "Autonomous robot navigation based on OpenStreetMap geodata," in *Proc. 13th Int. IEEE Conf. Intell. Transp. Syst.*, Sep. 2010, pp. 1645–1650.

[26] K. Klipp, A. Kisand, J. Wortmann, and I. Radusch, "Multidimensional in- and outdoor pedestrian tracking using OpenStreetMap data," in *Proc. Int. Conf. Indoor Positioning Indoor Navigat. (IPIN)*, Nov. 2021, pp. 1–8.

[27] R. J. Lisle, "Google Earth: A new geological resource," *Geol. Today*, vol. 22, no. 1, pp. 29–32, Jan. 2006.

[28] Z. Hu, P. K. Munneke, S. Lhermitte, M. Dirscherl, C. Ji, and M. van den Broeke, "FABIAN: A daily product of fractional austral-summer blue ice over Antarctica during 2000–2021 based on MODIS imagery using Google Earth engine," *Remote Sens. Environ.*, vol. 280, Oct. 2022, Art. no. 113202.

[29] S. Chen et al., "Monitoring temperate forest degradation on Google Earth engine using Landsat time series analysis," *Remote Sens. Environ.*, vol. 265, Nov. 2021, Art. no. 112648.

[30] L. Parente, V. Mesquita, F. Miziara, L. Baumann, and L. Ferreira, "Assessing the pasturelands and livestock dynamics in Brazil, from 1985 to 2017: A novel approach based on high spatial resolution imagery and Google Earth engine cloud computing," *Remote Sens. Environ.*, vol. 232, Oct. 2019, Art. no. 111301.

[31] Y. Choi and A. Nieto, "Optimal haulage routing of off-road dump trucks in construction and mining sites using Google Earth and a modified least-cost path algorithm," *Autom. Construction*, vol. 20, no. 7, pp. 982–997, Nov. 2011.

[32] G. Pulighe, V. Baiocchi, and F. Lupia, "Horizontal accuracy assessment of very high resolution Google Earth images in the city of Rome, Italy," *Int. J. Digit. Earth*, vol. 9, no. 4, pp. 342–362, Apr. 2016.

[33] X. W. Wang and F. Wang, "The precision of Google Earth map analysis with the coordinates of IGS stations," *Int. Arch. Photogramm., Remote Sens. Spatial Inf. Sci.*, vol. 42, pp. 1053–1056, Feb. 2020.

[34] J. Li and M. Wu, "The improvement of positioning accuracy with weighted least square based on SNR," in *Proc. 5th Int. Conf. Wireless Commun., Netw. Mobile Comput.*, Sep. 2009, pp. 1–4.

[35] L. Li, J. Zhong, and M. Zhao, "Doppler-aided GNSS position estimation with weighted least squares," *IEEE Trans. Veh. Technol.*, vol. 60, no. 8, pp. 3615–3624, Oct. 2011.

[36] M. S. Grewal, *Kalman Filtering*. Berlin, Germany: Springer, 2011.

[37] M. G. Petovello, K. O'Keefe, G. Lachapelle, and M. E. Cannon, "Consideration of time-correlated errors in a Kalman filter applicable to GNSS," *J. Geodesy*, vol. 83, no. 1, pp. 51–56, Jan. 2009.

[38] F. S. T. Van Diggelen, *A-GPS: Assisted GPS, GNSS, and SBAS*. Norwood, MA, USA: Artech House, 2009.

[39] G. Chen, *Approximate Kalman Filtering*. Singapore: World Scientific, 1993.

[40] T. Suzuki, "First place award winner of the smartphone decimeter challenge: Global optimization of position and velocity by factor graph optimization," in *Proc. 34th Int. Tech. Meeting Satell. Division Inst. Navigat. (ION GNSS)*, Oct. 2021, pp. 2974–2985.

[41] T. Suzuki, "1st place winner of the smartphone decimeter challenge: Two-step optimization of velocity and position using smartphone's carrier phase observations," in *Proc. ION GNSS Int. Tech. Meeting Satell. Division Inst. Navigat.*, Oct. 2022, pp. 2276–2286.

[42] W. Wen, T. Pfeifer, X. Bai, and L. T. Hsu, "Factor graph optimization for GNSS/INS integration: A comparison with the extended Kalman filter," *Navigat., J. Inst. Navigat.*, vol. 68, no. 2, pp. 315–331, 2021.

[43] P. Chao, Y. Xu, W. Hua, and X. Zhou, "A survey on map-matching algorithms," in *Proc. 31st Australas. Database Conf.*, Melbourne, VIC, Australia. Cham, Switzerland: Springer, Feb. 2020, pp. 121–133.

[44] M. A. Quddus, W. Y. Ochieng, and R. B. Noland, "Current map-matching algorithms for transport applications: State-of-the art and future research directions," *Transp. Res. C, Emerg. Technol.*, vol. 15, no. 5, pp. 312–328, Oct. 2007.

[45] M. Hashemi and H. A. Karimi, "A critical review of real-time map-matching algorithms: Current issues and future directions," *Comput., Environ. Urban Syst.*, vol. 48, pp. 153–165, Nov. 2014.

[46] J. S. Kim, J. H. Lee, T. H. Kang, W. Y. Lee, and Y. G. Kim, "Node based map matching algorithm for car navigation system," in *Proc. 29th ISATA Symp.*, vol. 10, 1996, pp. 121–126.

[47] L. Li, M. Quddus, and L. Zhao, "High accuracy tightly-coupled integrity monitoring algorithm for map-matching," *Transp. Res. C, Emerg. Technol.*, vol. 36, pp. 13–26, Nov. 2013.

[48] W. Wen and L.-T. Hsu, "Factor graph optimization for tightly-coupled GNSS pseudorange/Doppler/carrier phase/INS integration: Performance in urban canyons of Hong Kong," in *Proc. ION GNSS Int. Tech. Meeting Satell. Division Inst. Navigat.*, Oct. 2022, pp. 2178–2189.

[49] S. Das, R. Watson, and J. Gross, "Review of factor graphs for robust GNSS applications," 2021, *arXiv:2112.07794*.

[50] Y. Zhong, W. Wen, H.-F. Ng, X. Bai, and L.-T. Hsu, "Real-time factor graph optimization aided by graduated non-convexity based outlier mitigation for smartphone decimeter challenge," in *Proc. 35th Int. Tech. Meeting Satell. Division Inst. Navigat. (ION GNSS)*, 2022, pp. 2339–2348.

[51] A. M. Herrera, H. F. Suhandri, E. Realini, M. Reguzzoni, and M. C. de Lacy, "GoGPS: Open-source MATLAB software," *GPS Solutions*, vol. 20, no. 3, pp. 595–603, Jul. 2016.

[52] H.-F. Ng, G. Zhang, and L.-T. Hsu, "A computation effective range-based 3D mapping aided GNSS with NLOS correction method," *J. Navigat.*, vol. 73, no. 6, pp. 1202–1222, Nov. 2020.

[53] L.-T. Hsu et al., "Hong Kong UrbanNav: An open-source multisensory dataset for benchmarking urban navigation algorithms," *Navigat., J. Inst. Navigat.*, vol. 70, no. 4, 2023, Art. no. 602.

[54] N. Sünderhauf and P. Protzel, "Switchable constraints for robust pose graph SLAM," in *Proc. IEEE/RSJ IROS*, Oct. 2012, pp. 1879–1884.

[55] X. Xia, L.-T. Hsu, and W. Wen, "Integrity-constrained factor graph optimization for GNSS positioning," in *Proc. IEEE/ION Position, Location Navigat. Symp. (PLANS)*, Apr. 2023, pp. 414–420.

[56] N. Sünderhauf, M. Obst, S. Lange, G. Wanielik, and P. Protzel, "Switchable constraints and incremental smoothing for online mitigation of non-line-of-sight and multipath effects," in *Proc. IEEE Intell. Vehicles Symp. (IV)*, 2013, pp. 262–268.

[57] S. Agarwal and K. Mierle, "Ceres solver," Nov. 2019. [Online]. Available: http://ceres-solver.org

[58] J. J. Moré, "The Levenberg–Marquardt algorithm: Implementation and theory," in *Numerical Analysis*. Berlin, Germany: Springer, Jun. 2006, pp. 105–116.

[59] L.-T. Hsu et al., "UrbanNav: An open-sourced multisensory dataset for benchmarking positioning algorithms designed for urban areas," in *Proc. 34th Int. Tech. Meeting Satell. Division Inst. Navigat. (ION GNSS)*, Oct. 2021, pp. 226–256.

[60] H. Ng, G. Zhang, Y. Luo, and L. Hsu, "Urban positioning: 3D mapping-aided GNSS using dual-frequency pseudorange measurements from smartphones," *Navigation*, vol. 68, no. 4, pp. 727–749, Dec. 2021.

Yihan Zhong received the bachelor's degree in process equipment and control engineering from Guangxi University, Nanning, China, in 2020, and the master's degree from The Hong Kong Polytechnic University (PolyU), Hong Kong, in 2022, where he is currently pursuing the Ph.D. degree with the Department of Aeronautical and Aviation Engineering (AAE).

His research interests include collaborative positioning and low-cost localization.

Runzhi Hu (Graduate Student Member, IEEE) was born in Leshan, Sichuan, China. He received the B.S. and master's degrees in mechanical engineering and computer science from China Agricultural University, Beijing, China, in 2018 and 2021, respectively. He is currently pursuing the Ph.D. degree with The Hong Kong Polytechnic University, Hong Kong.

His research interests include HD map, multisensor fusion, SLAM, and GNSS positioning in urban canyons.

Li-Ta Hsu (Senior Member, IEEE) received the B.S. and Ph.D. degrees in aeronautics and astronautics from the National Cheng Kung University, Tainan City, Taiwan, in 2007 and 2013, respectively.

In 2012, he was a Visiting Scholar at University College London, London, U.K. He is currently an Associate Professor with the Department of Aeronautical and Aviation Engineering, The Hong Kong Polytechnic University, Hong Kong, before he served as a Post-Doctoral Researcher at the Institute of Industrial Science, University of Tokyo, Tokyo, Japan. His research interests include GNSS positioning in challenging environments and localization for pedestrians, autonomous driving vehicles, and unmanned aerial vehicles.

Xiwei Bai (Member, IEEE) received the Ph.D. degree from the Department of Aeronautical and Aviation Engineering (AAE), The Hong Kong Polytechnic University (PolyU), Hong Kong, in 2023.

Currently, she works as a Post-Doctoral Researcher at AAE, PolyU. Her research interests include visual-inertial odometry and visual-aided GNSS positioning for autonomous vehicle localization.

Weisong Wen (Member, IEEE) received the B.E. degree in mechanical engineering from Beijing Information Science and Technology University (BISTU), Beijing, China, in 2015, the M.E. degree in mechanical engineering from the China Agricultural University, Beijing, in 2017, and the Ph.D. degree in mechanical engineering from The Hong Kong Polytechnic University (PolyU), Hong Kong, in 2020.

He was also a Visiting Ph.D. Student with the Faculty of Engineering, University of California, Berkeley (UC Berkeley), Berkeley, CA, USA, in 2018. Before joining PolyU as an Assistant Professor, in 2023, he has been a Research Assistant Professor at AAE, PolyU, since 2021. He has authored or coauthored 30 SCI papers and 40 conference papers in the field of GNSS (ION GNSS+) and navigation for Robotic systems (IEEE ICRA, IEEE ITSC), such as autonomous driving vehicles.

Dr. Wen won the Innovation Award from TechConnect 2021, the Best Presentation Award from the Institute of Navigation (ION) in 2020, and the First Prize in the Hong Kong Section in the Qianhai-Guangdong-Macao Youth Innovation and Entrepreneurship Competition in 2019 based on his research achievements in 3-D LiDAR aided GNSS positioning for robotics navigation in urban canyons. The developed 3-D LiDAR-aided GNSS positioning method has been reported by top magazines such as Inside GNSS and has attracted industry recognition with remarkable knowledge transfer.

Xingxing Li received the B.Sc. degree from the School of Geodesy and Geomatics, Wuhan University, Wuhan, China, in 2012, and the Ph.D. degree from the Department of Geodesy and Remote Sensing, German Research Center for Geosciences (GFZ), Potsdam, Germany, in 2015.

He is currently a Professor at Wuhan University. His current research mainly involves GNSS precise data processing and its application for geosciences.